

Nanobubble Collapse on a Silica Surface in Water: Billion-Atom Reactive Molecular Dynamics Simulations

Adarsh Shekhar, Ken-ichi Nomura, Rajiv K. Kalia, Aiichiro Nakano, and Priya Vashishta*

Collaboratory for Advanced Computing and Simulations, Department of Chemical Engineering and Materials Science, Department of Physics and Astronomy, and Department of Computer Science, University of Southern California, Los Angeles, California 90089-0242, USA

(Received 19 June 2013; published 31 October 2013)

Cavitation bubbles occur in fluids subjected to rapid changes in pressure. We use billion-atom reactive molecular dynamics simulations on a 163 840-processor BlueGene/P supercomputer to investigate damage caused by shock-induced collapse of nanobubbles in water near an amorphous silica surface. Collapse of an empty bubble generates a high-speed nanojet, which causes pitting on the silica surface. We find pit radii are close to bubble radii, and experiments also indicate linear scaling between them. The gas-filled bubbles undergo partial collapse and, consequently, the damage on the silica surface is mitigated.

DOI: [10.1103/PhysRevLett.111.184503](https://doi.org/10.1103/PhysRevLett.111.184503)

PACS numbers: 47.55.D-, 31.15.xv, 62.50.Ef

Erosion due to bubble collapse is commonly observed in pipes, turbines, pumps, and ship propellers [1–5]. Haines *et al.* [6] have observed cavitation erosion damage in spallation neutron sources, where rapidly deposited heat energy from the proton beam generates pressure waves and cavitation bubbles in mercury [7]. Collapse of these bubbles can cause severe damage to the vessel wall, as reported by Lee *et al.* [8]. Sonoluminescence has also been reported in bubble collapse experiments [9]. Recent experiments by Zhang and collaborators [10] have indicated spatial heterogeneities in water inside a nanoporous silica matrix.

Recently, cavitation bubbles have been used beneficially in a number of technological applications. This includes an environmentally friendly approach to generate nanoporous or mesoporous material surfaces with acoustic cavitation [11,12]. In this approach, high-intensity focused ultrasound produces nano- or microbubbles. When bubbles collapse, high-speed nanojets or microjets of water are generated in an environment akin to that of a microreactor [13], i.e., extremely high temperatures and pressures in a localized volume while the rest of the system is under ambient conditions. The impact of high-speed jets and oxidation due to water sonolysis can make the metal surface porous at the nanometer scale. By controlling the ultrasound intensity and frequency and by varying the solvent and sonication time, it is possible to control the roughness and porosity of sponges on the surfaces of various metals and metallic alloys. Mesoporous sponges are excellent stimuli-responsive systems to encapsulate and deliver a variety of active compounds including corrosion inhibitors, antibodies, DNA fragments, enzymes, and biocides [11]. Ultrasound-assisted cavitation is also used in medical applications such as dentistry and extracorporeal shock-wave treatment of renal stones [14]. Ultrasound, with *in vivo* gas bubbles, is used to enhance the permeability of cell membranes [15] and thus improve the efficiency of protein, DNA, and drug delivery.

Cavitation bubbles are also used beneficially in an industrial process called water jet peening [16] in nuclear reactors. Pressurized water is injected into water, generating cavitation bubbles. The pressure released during the bubble collapse mitigates the residual tensile stress and prevents stress corrosion cracking in austenite-based stainless steel and nickel based alloys used in nuclear reactors.

Collapse of a cavitation bubble near a solid has been captured with high-speed cinematography [17,18], but with limited spatial resolution (\sim a few micrometers). Philipp and Lauterborn [19] have observed experimentally that the shock generated by the collapse of acoustic cavitation bubbles is strongly attenuated with the distance, H_0 , between the bubble and the solid surface, and that for maximum damage, H_0 should be less than twice the initial bubble radius R_0 . The experiment reveals that the diameter of the damaged area scales with the bubble radius. Bubble collapse has also been studied by Johnsen and Colonius [20] with continuum simulation [21] approaches and the impact damage of bubble collapse on solid surfaces has been mapped out as a function of the stand-off parameter, $s_d = H_0/R_0$ [see Fig. 1(a)]. These simulations also show that the pressure generated on the wall due to shock-induced bubble collapse is maximum for $s_d = 2$. Strachan *et al.* have found that shock loading can initiate chemical decomposition of materials [22].

Despite a great deal of research on cavitation bubbles, several important questions about bubble collapse near a solid surface remain unanswered: Is there turbulence at the nanoscale during bubble collapse and if there is, what are its characteristics? What is the extent of mechanical damage due to nanojet impact and how does it scale with the bubble size? What is the nature of chemical damage? What is the connection between chemical and mechanical damages? Quantum mechanical calculations by Lorenz *et al.* [23] have revealed that the structure of water near a silica surface is different from that of bulk. Lane and collaborators have

carried out molecular dynamics simulations to study water-induced damage in self-assembled monolayers on amorphous silica [24].

In this Letter, we examine chemical and mechanical damages through billion-atom reactive molecular dynamics (MD) simulations [25] of shock-induced collapse of a nanobubble near a silica slab. The simulations were performed on the full BlueGene/P supercomputer (163 840 processors) at the Argonne Leadership Computing Facility. Details of the interatomic potential and experimental validation are given in the Supplemental Material [26]. In the billion-atom MD simulations, the system consists of a 60 nm thick silica slab placed in an MD box of dimensions $285 \times 200 \times 200 \text{ nm}^3$ in the x , y , and z directions respectively; see Fig. 1(a). The rest of the MD box contains water molecules and a spherical nanobubble of diameter 97.6 nm. The initial distance between the center of the bubble and the silica surface is 90 nm, and the stand-off parameter, $s_d = 1.84$. We applied shock with a particle velocity of 2 km/s and found the shock velocity in water to be 5 km/s. This is in good agreement with experimental data of Rybakov [27] and the MD simulation results of Vedadi *et al.* [28]. We used periodic boundary conditions normal to the direction of shock-wave propagation ($-x$). The equations of motion were integrated with the velocity-Verlet algorithm using a time step of 0.5 fs.

Figure 1(b) shows the shock wave in water, traveling from right to left, before it hits the nanobubble. The density of water in the shock region is 1.5 g/cc and the pressure is 10 GPa. The MD simulation reveals that the structure of water has changed significantly in the shock region; e.g., on average, the number of nearest neighbors of a water molecule has increased from 4 to 8. When the shock front hits the nanobubble, water molecules at the periphery of the bubble rush in to form a focused nanojet in the direction of the shock-wave propagation. Figure 2(a) shows a partially collapsed nanobubble and the nanojet at time $t = 20 \text{ ps}$, and Fig. 2(b) shows the nanojet velocity streamlines shortly before the bubble collapses completely. The nanojet reaches a speed of 7.8 km/s, which is significantly

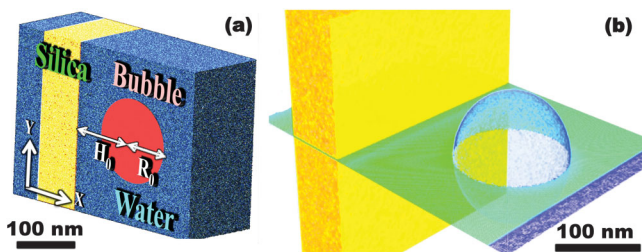


FIG. 1 (color). (a) Schematic diagram of the initial setup of the system. Oxygen and hydrogen atoms in water are shown as blue and cyan dots, respectively. (b) Snapshot of the system at time $t = 5 \text{ ps}$. In the central slice through the silica slab, the color green represents normal water and dark blue is the incoming shock wave in water. The bubble surface is shown in blue.

higher than the shock velocity (5 km/s). Experimentally, Ohl and Ikink have observed similar jetting phenomenon in the collapse of micron-size bubbles [13]. They find the microjet length is approximately three times the initial bubble radius. Kodama and Tomita find a similar scaling relation for bubbles of radii between 0.1 and 1 mm [29]. Together with our previous simulation results on nanometer size bubbles [28], these experiments suggest that the scaling relation between the jet length and bubble radius holds for a wide range of bubble sizes. Experimental results of Kodama and Takayama [30] indicate that the ratio between the size of the damaged pit on a gelatin surface to bubble radius is close to 0.1, whereas we find this ratio to be 0.3.

Chemical activity in water increases significantly with the onset of bubble collapse and nanojet formation. We observe an increase in the hydronium ion production with the nanojet growth. The blue curve in Fig. 2(c) shows the spatial distribution of H_3O^+ ions along the direction of nanojet propagation (i.e., along $-x$). The H_3O^+ ions are counted in voxels of dimensions $1 \times 5 \times 5 \text{ nm}^3$ around the nanojet. At $t = 25 \text{ ps}$, the H_3O^+ population peaks at the location of the shock front inside the nanobubble. We observe an increase in the number of H_3O^+ ions when the nanojet hits the distal side of the bubble at 202 nm. The red curve in Fig. 2(c) shows the spatial distribution of hydronium ions just when the bubble collapses completely. The peak in the red curve at 218 nm is due to a secondary shock wave generated by the nanojet impact on the distal

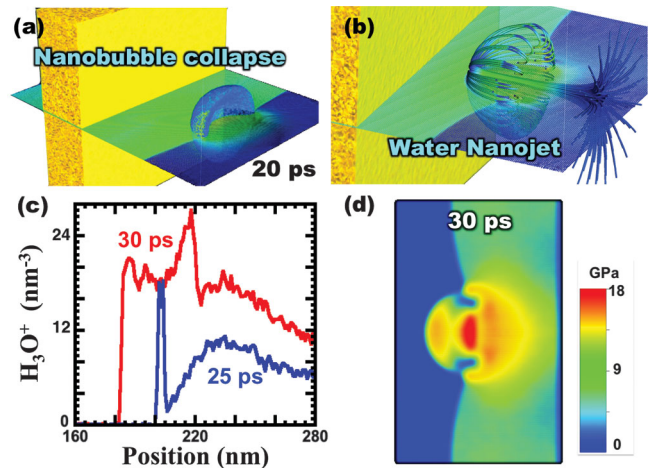


FIG. 2 (color). (a) Partially collapsed nanobubble under the influence of shock wave at time $t = 20 \text{ ps}$. (b) Water nanojet formed during shock-induced collapse of the nanobubble. The silica slab is shown in yellow. The central slice across the silica slab is color coded by the magnitude of the velocity of water molecules. The velocity field lines show a focused jet of water molecules. (c) Number of H_3O^+ species along the central slice of the system. H_3O^+ ion production increases significantly when the nanojet hits the distal side of the bubble at time $t = 25 \text{ ps}$. (d) Pressure profile in water at $t = 30 \text{ ps}$ shows a secondary shock wave.

side of the bubble. The secondary shock propagates in the direction opposite to the primary shock wave. The pressure profile of the secondary shock at time $t = 30$ ps is shown in Fig. 2(d). The peak pressure in the secondary shock wave (18 GPa) is larger than the pressure in the nanojet.

The nanojet impact on the silica slab initiates pit damage at $t = 35$ ps; see Fig. 3(a). At 50 ps the shock wave has already crossed the silica slab, leaving behind a pit of diameter 78 nm and depth 17.5 nm. Figures 3(b) and 3(c) show the spatial distributions of the hydronium ion and the pressure in the system at time $t = 50$ ps. The peak pressure (18 GPa) agrees very well with the estimate of water-hammer pressure, $P = \rho cv$, where ρ is the mass density, c is the speed of sound, and v is the jet speed [17]. Taking the sound velocity in water to be 1.5 km/s, and using the values $\rho = 1.5$ g/cc and $v \approx 7.8$ km/s from our simulations, we estimate water-hammer pressure to be ~ 18 GPa. The number of hydronium ions decreases as the pressure decreases, reaching a minimum value of 9 GPa around 200 nm. The pressure profile in Fig. 3(c) shows that the pressure in the reflected shock wave in the silica slab reaches a maximum value of 18 GPa around 235 nm and, correspondingly, Fig. 3(b) has a peak in the spatial distribution of the hydronium ions. Virot *et al.* have observed similar erosion damage on fused silica and soda lime glass due to acoustic cavitation at the water-silica interface [12].

To quantify mechanical damage in the system, we calculated the volume of the cavitation pit in the silica slab. For comparison, we performed another MD simulation on a system with 100 million atoms. The initial diameter of the bubble was 40 nm and the stand-off parameter was the same as in the case of the billion-atom MD simulation. Figure 4(a) shows the pits in silica resulting from nanojet impact in the billion-atom and 100 million-atom systems. The cavitation pit is a portion of a sphere. In the case of a billion-atom system with a bubble of radius of 49 nm, the

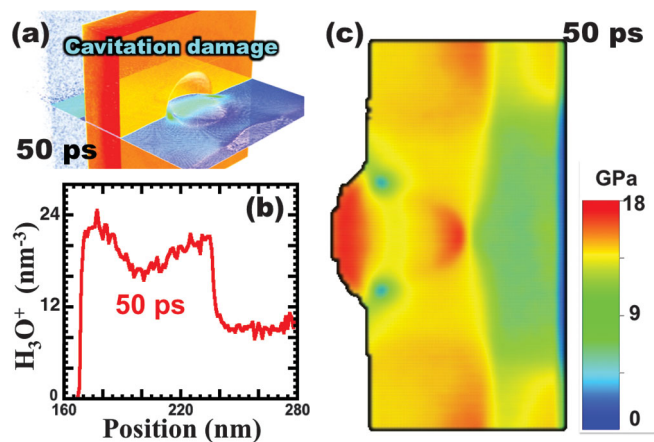


FIG. 3 (color). (a) Snapshot of cavitation damage in the silica slab due to nanobubble collapse at time $t = 50$ ps. (b) Spatial distribution of H_3O^+ ions in the water nanojet. (c) Pressure profile at $t = 50$ ps shows the reflected shock wave in water. The peaks in (b) correspond to the high-pressure region in (c).

pit is a portion of a sphere of radius 50 nm. In the case of a 100 million-atom system containing a bubble of radius 20 nm, the sphere corresponding to the damage pit has a radius of 23 nm. These results indicate that the radius of the damage pit is close to the bubble radius. Experiments on damage caused by the collapse of millimeter size bubbles also indicate that the diameter of the damaged area scales with the bubble radius [19]. Figure 4(b) shows an atomistic view of a 0.5 nm thick slice at the center of the damaged silica network after the nanojet impact at time $t = 50$ ps. We observe a large number of hydrogen forming bonds with Si and O in the damaged region of the silica slab. To quantify chemical damage, we show in Fig. 4(c) the distribution of SiOH species in 1 nm deep annular disks centered at the damage pit. The radial distance between successive annular disks is 1 nm. The red and blue curves show SiOH distributions in the 100 million-atom and 1 billion-atom systems. Initially the number of SiOH groups on the surface was ~ 6 nm^{-2} . After the shock wave crosses the silica slab we observe a considerable increase in the population of SiOH, which peaks around the pit edge.

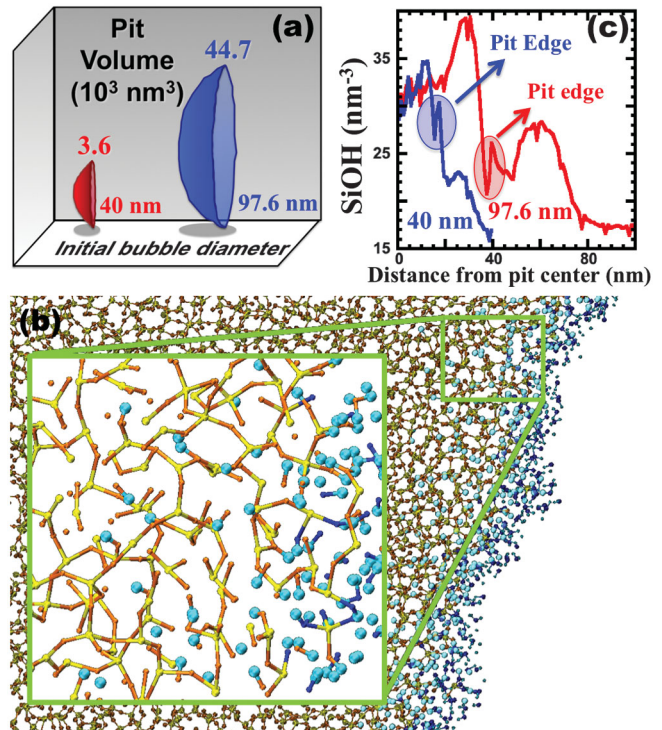


FIG. 4 (color). (a) Volumes of cavitation pits in systems with nanobubbles of diameter 40 nm (red) and 97.6 nm (blue). (b) Snapshot shows atoms at the pit edge of the silica slab in the system with 10^9 atoms. Silicon-oxygen bonds are yellow-orange, and cyan spheres represent hydrogen atoms inside the silica slab. Blue spheres represent oxygen atoms in water molecules within 0.5 nm from the silica slab. (c) Silanol distribution in the silica slab as a function of the distance from the pit center for bubbles of diameters 40 nm (red) and 97.6 nm (blue). The pit center is defined as the center of the projection of the cavitation pit on the plane normal to the shock direction.

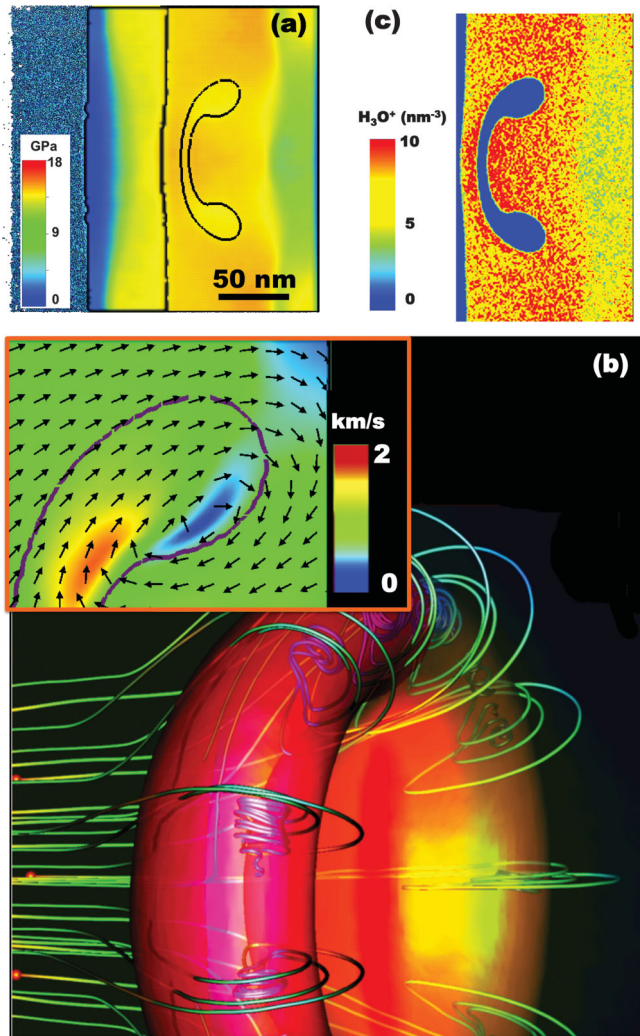


FIG. 5 (color). (a) Shock-induced deformation of a gas-filled nanobubble and the pressure distribution in a cross section of the system. (b) Snapshot of vortex rings at the periphery of the nanobubble. Streamlines represent molecular velocities, and the inset shows the velocity field of water molecules (black arrows) around the edge of the deformed bubble. (c) Number of H_3O^+ ions per nm^3 around the partially collapsed gas-filled bubble at time $t = 50$ ps.

Experimentally, Virot *et al.* have observed chemical leeching in silica glass due to cavitation bubbles [12].

We also performed two sets of simulations in which the nanobubble contained an inert gas at a density of 0.24 g/cc. This value of the gas density stabilizes the bubble, keeping it in equilibrium with water. The role of gas density in the stability of a single bubble is usually examined [31] for gas densities around 0.5 g/cc. The simulated systems contained 10^9 and 10^8 atoms and the initial bubble radii in these systems were again 97.6 and 40 nm, respectively. The stand-off parameter and the particle velocity were the same as before ($s_d = 1.84$, $v_p = 2$ km/s).

Figure 5(a) shows pressure distribution in and around the toroid-shaped deformed gas-filled bubble in the billion-atom

system after the shock wave crosses the silica slab ($t = 50$ ps). Similar toroid-shaped deformation has also been seen in shock-wave experiments by Ranjan *et al.* on spherical and cylindrical inhomogeneities [32], and in continuum simulations of shock-induced collapse of a bubble near a wall by Johnsen and Colonius [20]. We find the nanobubble shape change is due to vortices at the periphery of the gas bubble; see Fig. 5(b). Here the velocity field is represented by streamlines around the deformed gas bubble and color coded by magnitude. These vortices are generated by the gradients in pressure [see Fig. 5(a)] and density at the periphery of the collapsing nanobubble. Experiments by Ranjan *et al.* also reveal the formation of vortex rings from pressure and density gradients generated by the collapse of gas-filled bubbles in three dimensions [32]. The inset in Fig. 5(b) shows the velocity vectors in the region of vortex rings. Since the density of the nanobubble is less than that of the medium, the vortex rings at the bubble periphery rotate towards the center of the bubble. This has also been observed in continuum simulations for bubble density less than that of the medium [32]. Water-hydrophobic interface is known to be chemically active [33]. Figure 5(c) shows the chemical activity generated by the partial collapse of the gas-filled nanobubble. As shown in the figure, the hydronium ion production is mostly in the central region of the collapsed bubble and around the vortex rings.

In the case of a gas-filled bubble, the mechanical damage in silica is less compared to the damage caused by the collapse of an empty bubble. This is consistent with the experimental observation of Ida *et al.* that gas-filled nanobubbles suppress cavitation erosion damage in liquid mercury [7]. In Fig. 5(a), the silica slab is overlaid with the pressure distribution normal to the silica slab. In the case of an empty bubble, the pressure in the pit region decreases as the distance from the pit center increases, whereas in the case of a gas-filled bubble the pressure is more uniformly distributed.

In summary, large-scale reactive MD simulations of shock-induced nanobubble collapse reveal an increase in the number of hydronium ions when the nanobubble begins to collapse and water molecules from the bubble periphery rush in to form a focused jet. The nanojet impact on the distal side of the collapsing nanobubble generates a large number of hydronium ions and a secondary shock wave. When the nanojet hits the silica surface, it creates a reflected shock wave and a damaged pit whose radius is close to the bubble radius. We observe a large number of silanol and hydronium ions in the pit. We also performed reactive MD simulations with gas-filled nanobubbles of the same dimensions and for the same value of the stand-off parameter. These nanobubbles do not collapse completely nor do they cause much damage to the silica surface because the nanojets are much weaker than the nanojets from the collapse of empty bubbles. Pressure and density gradients around partially collapsed gas-filled nanobubbles

give rise to vortex rings and enhance hydronium ion production.

This work was supported by DOE-BES Theoretical Condensed Matter Physics Grant No. DE-FG02-04ER46130. The computing resources were provided by a DOE—Innovative and Novel Computational Impact on Theory and Experiment (INCITE) Grant. We thank Paul Messina, Nichols Romero, William Scullin, and the support team of Argonne Leadership Computing Facility for scheduling 67 million core hours in units of 60-h blocks on full BlueGene/P for the simulations and Joseph Insley, Argonne Visualization Center for helping with the visualization.

*To whom all correspondence should be addressed.

- [1] E. A. Brujan, K. Nahen, P. Schmidt, and A. Vogel, *J. Fluid Mech.* **433**, 251 (2001).
- [2] A. Karimi and J. L. Martin, *Int. Mater. Rev.* **31**, 1 (1986).
- [3] B. Karunamurthy, M. Hadfield, C. Vieillard, and G. E. Morales-Espejel, *Tribol. Int.* **43**, 2251 (2010).
- [4] A. Vogel, W. Lauterborn, and R. Timmi, *J. Fluid Mech.* **206**, 299 (1989).
- [5] R. E. A. Arndt, *Annu. Rev. Fluid Mech.* **13**, 273 (1981).
- [6] J. R. Haines, B. W. Riemer, D. K. Felde, J. D. Hunn, S. J. Pawel, and C. C. Tsai, *J. Nucl. Mater.* **343**, 58 (2005).
- [7] M. Ida, T. Naoe, and M. Futakawa, *Phys. Rev. E* **76**, 046309 (2007).
- [8] M. Lee, Y. Kim, Y. Oh, Y. Kim, S. Lee, H. Hong, and S. Kim, *Wear* **255**, 157 (2003).
- [9] D. Schanz, B. Metten, T. Kurz, and W. Lauterborn, *New J. Phys.* **14**, 113019 (2012).
- [10] Y. Zhang, A. Faraone, W. A. Kamitakahara, K. H. Liu, C. Y. Mou, J. B. Leão, S. Chang, and S. H. Chen, *Proc. Natl. Acad. Sci. U.S.A.* **108**, 12 206 (2011).
- [11] D. V. Andreeva, D. V. Sviridov, A. Masic, H. Möhwald, and E. V. Skorb, *Small* **8**, 820 (2012).
- [12] M. Viot, T. Chave, S. I. Nikitenko, D. G. Shchukin, T. Zemb, and H. Möhwald, *J. Phys. Chem. C* **114**, 13 083 (2010).
- [13] C. D. Ohi and R. Ikink, *Phys. Rev. Lett.* **90**, 214502 (2003).
- [14] M. Delius, F. Ueberle, and W. Eisenmenger, *Ultrasound Med. Biol.* **24**, 1055 (1998).
- [15] A. Choubey, M. Vedadi, K. Nomura, R. K. Kalia, A. Nakano, and P. Vashishta, *Appl. Phys. Lett.* **98**, 023701 (2011).
- [16] Hitachi-GE, *E-Journal of Advanced Maintenance* **1**, NT7 (2009).
- [17] N. K. Bourne and J. E. Field, *J. Appl. Phys.* **78**, 4423 (1995).
- [18] W. Lauterborn and W. Hentschel, *Ultrasonics* **23**, 260 (1985).
- [19] A. Philipp and W. Lauterborn, *J. Fluid Mech.* **361**, 75 (1998).
- [20] E. Johnsen and T. Colonius, *J. Fluid Mech.* **629**, 231 (2009).
- [21] S. Succi, G. Smith, and E. Kaxiras, *J. Stat. Phys.* **107**, 343 (2002).
- [22] A. Strachan, A. C. T. van Duin, D. Chakraborty, S. Dasgupta, and W. A. Goddard, III, *Phys. Rev. Lett.* **91**, 098301 (2003).
- [23] C. D. Lorenz, M. Tsige, S. B. Rempe, M. Chandross, M. J. Stevens, and G. S. Grest, *J. Comput. Theor. Nanosci.* **7**, 2586 (2010).
- [24] J. M. D. Lane, M. Chandross, C. D. Lorenz, M. J. Stevens, and G. S. Grest, *Langmuir* **24**, 5734 (2008).
- [25] S. Yip, *Handbook of Materials Modeling* (Springer, New York, 2005).
- [26] See Supplemental Material at <http://link.aps.org/supplemental/10.1103/PhysRevLett.111.184503> for details about the preparation of the system, the interatomic potential used and its validation, simulation conditions, and simulation movies.
- [27] A. P. Rybakov, *J. Appl. Mech. Tech. Phys.* **37**, 629 (1996).
- [28] M. Vedadi, A. Choubey, K. Nomura, R. K. Kalia, A. Nakano, P. Vashishta, and A. C. T. van Duin, *Phys. Rev. Lett.* **105**, 014503 (2010).
- [29] T. Kodama and Y. Tomita, *Appl. Phys. B* **70**, 139 (2000).
- [30] T. Kodama and K. Takayama, *Ultrasound Med. Biol.* **24**, 723 (1998).
- [31] L. Yuan, C. Y. Ho, M.-C. Chu, and P. T. Leung, *Phys. Rev. E* **64**, 016317 (2001).
- [32] D. Ranjan, J. Oakley, and R. Bonazza, *Annu. Rev. Fluid Mech.* **43**, 117 (2011).
- [33] K. N. Kudin and R. Car, *J. Am. Chem. Soc.* **130**, 3915 (2008).